













Constraining Inputs to Realistic Kilonova Simulations through Comparison to Observed r -process Abundances

Marko Ristić¹ , Erika M. Holmbeck^{2,3,12} , Ryan T. Wollaeger^{4,5} , Oleg Korobkin^{4,6} , Elizabeth Champion⁷ , Richard O’Shaughnessy¹ , Chris L. Fryer^{4,5,8,9,10} , Christopher J. Fontes^{4,11} , Matthew R. Mumpower^{3,4,6} , and Trevor M. Sprouse^{3,4,6} 

¹ Center for Computational Relativity and Gravitation, Rochester Institute of Technology, Rochester, NY 14623, USA; mr3364@rit.edu

² Observatories of the Carnegie Institution for Science, Pasadena, CA 91101, USA

³ Joint Institute for Nuclear Astrophysics—Center for the Evolution of the Elements, USA

⁴ Center for Theoretical Astrophysics, Los Alamos National Laboratory, Los Alamos, NM 87545, USA

⁵ Computer, Computational, and Statistical Sciences Division, Los Alamos National Laboratory, Los Alamos, NM 87545, USA

⁶ Theoretical Division, Los Alamos National Laboratory, Los Alamos, NM 87545, USA

⁷ Department of Physics and Astronomy, University of Rochester, Rochester, NY 14627, USA

⁸ The University of Arizona, Tucson, AZ 85721, USA

⁹ Department of Physics and Astronomy, The University of New Mexico, Albuquerque, NM 87131, USA

¹⁰ The George Washington University, Washington, DC 20052, USA

¹¹ Computational Physics Division, Los Alamos National Laboratory, Los Alamos, NM 87545, USA

Received 2023 June 26; revised 2023 August 8; accepted 2023 August 23; published 2023 October 9

Abstract

Kilonovae, one source of electromagnetic emission associated with neutron star mergers, are powered by the decay of radioactive isotopes in the neutron-rich merger ejecta. Models for kilonova emission consistent with the electromagnetic counterpart to GW170817 predict characteristic abundance patterns, determined by the relative balance of different types of material in the outflow. Assuming that the observed source is prototypical, this inferred abundance pattern in turn must match r -process abundances deduced by other means, such as what is observed in the solar system. We report on analysis comparing the input mass-weighted elemental compositions adopted in our radiative transfer simulations to the mass fractions of elements in the Sun, as a practical prototype for the potentially universal abundance signature from neutron star mergers. We characterize the extent to which our parameter inference results depend on our assumed composition for the dynamical and wind ejecta and examine how the new results compare to previous work. We find that a dynamical ejecta composition calculated using the FRDM2012 nuclear mass and FRLDM fission models with extremely neutron-rich ejecta ($Y_e = 0.035$) along with moderately neutron-rich ($Y_e = 0.27$) wind ejecta composition yields a wind-to-dynamical mass ratio of $M_w/M_d = 0.47$, which best matches the observed AT2017gfo kilonova light curves while also producing the best-matching abundance of neutron capture elements in the solar system, though, allowing for systematics, the ratio may be as high as of order unity.

Unified Astronomy Thesaurus concepts: [Nucleosynthesis \(1131\)](#); [R-process \(1324\)](#)

1. Introduction

For nearly half a century, neutron star binaries have been known to exist in nature, stemming from the first detection of a binary pulsar system (Hulse & Taylor 1975). Shortly thereafter, the general relativistic prediction of gravitational radiation from a compact object binary was measured in the same system, implying the possibility of neutron star binary coalescence (Taylor & Weisberg 1982). Recently, neutron star mergers were confirmed as astrophysical sources of both gravitational wave and electromagnetic emission with the detection of the binary neutron star merger GW170817 and its transient electromagnetic counterpart AT2017gfo (Tanvir et al. 2017; The LIGO Scientific Collaboration et al. 2017a, 2017b, 2017c, 2017d).

Around the same time as the first pulsar binary detection, compact object mergers involving neutron stars, either a binary

neutron star (BNS) or a black hole–neutron star (BHNS), were predicted to be candidates for rapid neutron capture (r -process) nucleosynthesis (Lattimer & Schramm 1974, 1976; Symbalisty & Schramm 1982; Eichler et al. 1989). The nuclei synthesized in the immediate aftermath of the post-merger ejecta were thought to be heavy ($A > 140$), with a sizable fraction of radioactive isotopes having short lifetimes owing to their instability (Rosswog 2015). As these nuclei decay, they release energy into the surrounding matter that would be emitted as ultraviolet, optical, and infrared thermal radiation once the ejecta becomes optically thin (Li & Paczyński 1998; Kulkarni 2005; Metzger et al. 2010). This thermal emission is now commonly referred to as a kilonova (Metzger 2019) and serves as the bridge between the r -process elements produced by neutron star mergers and their resultant electromagnetic emission (Goriely et al. 2011; Roberts et al. 2011; Korobkin et al. 2012; Metzger & Berger 2012; Cowan et al. 2021). Aside from the transient electromagnetic kilonova emission (including a gamma-ray burst; Abbott et al. 2017; Savchenko et al. 2017), r -process material ejecta from neutron star binary mergers like GW170817 could produce another observable signature: relic r -process abundances such as in ancient, metal-poor stars and in our solar system.

¹² Hubble Fellow.

Modeling kilonova light curves from merger events as viewed from the solar system by a distant observer requires the ejecta mass, velocity, composition, morphology, and viewing angle to be known, or otherwise supplied as model inputs. It has been conclusively demonstrated that the multiband light curves of AT2017gfo are poorly fit with single-component models, i.e., models consisting of a single type of ejecta described by fixed velocity, mass, and composition (Cowperthwaite et al. 2017). Instead, the AT2017gfo light curve is better fit by two (or even three) components describing multiple types of ejecta: generally, a high-opacity “dynamical” component, and a low-opacity “wind” component (Cowperthwaite et al. 2017; Tanvir et al. 2017; Troja et al. 2017; Villar et al. 2017).

In two-component models of kilonovae, the low-opacity wind component typically includes elements only up to the “second r -process peak” at $A \sim 130$, while the higher-opacity dynamical component includes even heavier elements (Nicholl et al. 2017; Pian et al. 2017; Miller et al. 2019). While these composition trends set a general opacity scale (see, e.g., Tanaka et al. 2020), the full details of the composition effects on electromagnetic emission depend on the components’ nuclear physics considerations, as well as their physical parameterizations described, in part, by the components’ masses M_d, M_w , and velocities v_d, v_w , where “ d ” and “ w ” refer to the dynamical and wind components, respectively. Previous studies of kilonovae have highlighted the importance of nuclear physics inputs on r -process nucleosynthesis and the resultant effect on observed kilonova emission (Barnes et al. 2021; Zhu et al. 2021). In this work, we build on previous studies by considering the effect that nuclear physics uncertainties have on parameter inference from kilonova light curves.

This work presents two-component nucleosynthetic yield constraints assuming r -process contribution exclusively from neutron star mergers and electromagnetic constraints assuming that all neutron star mergers are phenomenologically similar to GW170817.

Although neutron star mergers are frequently cited as the dominant source of r -process nucleosynthesis (Cowperthwaite et al. 2017; Thielemann et al. 2017), additional phenomena, such as collapsars, can launch r -process-rich outflows, indicating an additional source of nucleosynthesis (Barnes & Metzger 2022). At present, the r -process contribution of collapsars is not thought to be substantial enough to rival neutron star mergers as the dominant r -process nucleosynthesis channel (Bartos & Márka 2019; Macias & Ramirez-Ruiz 2019; Fraser & Schönrich 2022). In a similar vein, Skúladóttir (2020) find that at least two nucleosynthesis channels with different formation timescales are required to explain the presence of r -process elements at earlier times (≤ 100 Myr). While neutron star mergers are not excluded from consideration as the sole nucleosynthesis channel, they do require a short-timescale formation mechanism that is unexplained as of yet (Shen et al. 2015; Skúladóttir 2020). For simplicity, in this work we assume neutron star mergers as the sole r -process nucleosynthesis channel.

Likewise, we assume that the nucleosynthetic yields from AT2017gfo are prototypical of all kilonovae; however, Kawaguchi et al. (2020) and Barnes et al. (2021) highlight the significant effects that the post-merger remnant, mass ejection, and nuclear physics, among other things, can have on the nucleosynthesis and resultant observed light curves. In using the solar r -process abundances, we constrain the average

abundance of the population of neutron star mergers, with the assumption that AT2017gfo abundances are close to this average.

We investigate the effects of comparing elemental abundances from kilonova simulations to solar r -process abundances under the assumption that the second ($A \sim 130$) and third ($A \sim 195$) r -process peaks follow universal behavior, which is justified by the robustness of the r -process pattern observed among metal-poor stars (e.g., Sneden et al. 1994; Hill et al. 2002; Sneden et al. 2003; Frebel et al. 2007; Siqueira Mello et al. 2013; Lorusso et al. 2015). We use this comparison to create a parameter estimation prior driven by explicit consideration of r -process elemental abundances in kilonova ejecta to gauge the effects on recovered ejecta properties, i.e., the masses and velocities of the ejecta components. As kilonova models improve in complexity and more observations become available for parameter estimation purposes, we can use more representative simulation abundances to hone this prior in future studies.

In this work, we will assess the extent to which our assumptions about the ejected material are simultaneously consistent with both types of aforementioned observations. Specifically, we will examine whether the abundances produced by our nucleosynthesis simulations realistically match the r -process abundances observed in the Sun while simultaneously reproducing the AT2017gfo light curve as well. In Section 2.1, we discuss the radiative transfer, atomic, and nuclear physics codes used to calculate the surrogate light curves, line-binned opacities, and ejecta compositions, respectively, considered in this work. In Section 2.2, we describe our method of comparing mass-weighted r -process abundances from our simulations with the solar abundance pattern. Section 2.3 describes our parameter estimation framework and the effects of the r -process prior introduced in this work. In Section 3 we discuss whether the inclusion of the r -process prior makes a substantial difference in the parameter estimation process compared to prior work.

Our proof-of-concept analysis provides two key new approaches to multimessenger inference of BNS mergers. On the one hand, we provide a method to quantitatively assess the hypothesis of a universal r -process origin in BNS mergers with observations of kilonovae, by requiring consistent predictions for the ejecta’s electromagnetic emission and its asymptotic impact on r -process abundances. On the other hand, if the universal origin of r -process abundances is from binary neutron star mergers, our method can sharply refine our inferences about the ejected material. While in our proof-of-concept calculation we currently employ the Sun’s r -process abundances as a prototype for a pristine, universal abundance signature from BNS mergers, our method should ideally be applied to ongoing and future efforts to disentangle the BNS merger’s natal abundance contribution, for example, from isolated metal-poor stars or from abundance principal component correlations.

2. Methods

2.1. Simulation Setup

The aforementioned model abundances are not sufficient to create a direct link to kilonova electromagnetic emission on their own. However, they restrict which radioactive isotopes can plausibly exist and determine the radioactive heating rates

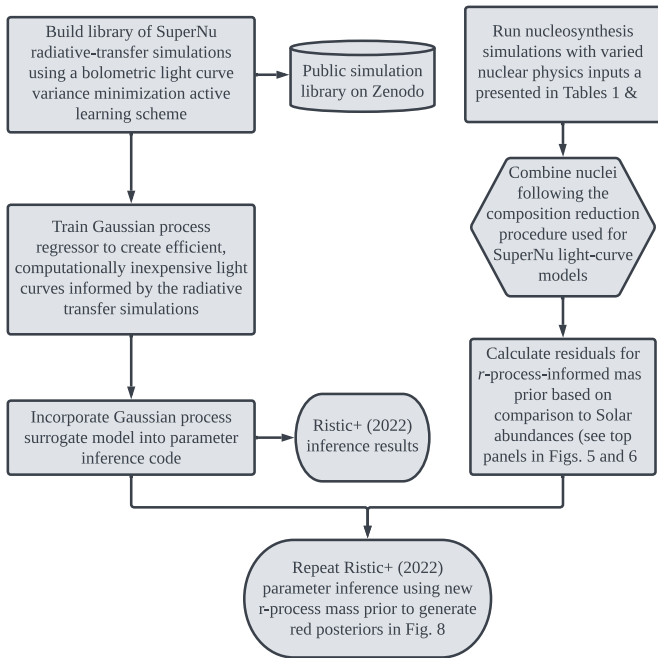


Figure 1. Unified Modeling Language (UML) diagram describing the large-scale steps taken in creating the r -process mass prior and using it during parameter inference to generate the red posteriors in Figure 8. Per standard UML definition, rectangles represent processes, cylinders represent databases, hexagons represent data preparation steps, and ovals represent terminators, or final products.

powering the kilonova at different times. In this section, we describe the details of our ejecta compositions, the relevant thermalization efficiencies, and the composition-dependent ejecta opacity effects that constitute our kilonova emission model. Figure 1 schematically shows the subsequent process for using these models to perform kilonova parameter inference.

Throughout this work, we assume a two-component kilonova model composed of a lanthanide-rich “dynamical” ejecta component and a lanthanide-poor “wind” ejecta component. Each of our two ejecta components, dynamical and wind, is described by a fixed morphology and elemental composition. The morphologies are fixed to torus shaped and peanut shaped for the dynamical and wind ejecta, respectively (as defined in Korobkin et al. 2021). The wind component compositions, contributing to elements around and between the first ($A \sim 80$) and second ($A \sim 130$) r -process peaks, are fixed in this study and are described by the H5 and H1 tracers in Perego et al. (2014) for the “wind1” and “wind2” models, respectively. We consider two different wind models with lower (wind1) and higher (wind2) neutron richness to gauge the effects of lighter- and heavier-element contributions in our comparison to solar r -process abundances. The dynamical ejecta compositions, composed of the elements from the second to the third r -process peak and beyond, are varied as described in Table 1; the dynamical ejecta composition used in our previous study, marked with an asterisk, is described by the model B tracer in Rosswog et al. (2014).

We use the models from our previous study (see Ristic et al. 2022) using `SuperNu`, a Monte Carlo code for simulation of time-dependent radiation transport with matter in local thermodynamic equilibrium (Wollaeger & van Rossum 2014). Our light-curve simulations use radioactive power sources

Table 1
Wind-to-dynamical Mass Ratios Sorted by Increasing Minimum Residuals for Each Dynamical Composition Considered

Mass Model	Fission Model	Y_e $\left(\frac{n_p}{n_p + n_n}\right)$	Wind Comp.	Mass Ratio (M_w/M_d)	Min. Residual (r_{\min})
FRDM2012	FRLDM	0.035	wind2	0.47	1257
FRDM2012	50/50	0.180	wind2	0.35	1849
FRDM2012	FRLDM	0.035	wind1	0.20	2001
HFB24	FRLDM	0.035	wind2	0.52	2470
FRDM2012 (*)	Panov	0.035	wind2	0.24	2550
	+				
	(2010)				
HFB24	FRLDM	0.180	wind2	0.19	2722
HFB24	FRLDM	0.035	wind1	0.10	2872
FRDM2012	50/50	0.180	wind1	17.07	3323
FRDM2012	Panov	0.035	wind1	17.69	4048
	+				
	(2010)				
HFB24	FRLDM	0.180	wind1	12.66	4192

Note. Mass ratios were determined by calculating the mean mass ratio of the bottom 2nd percentile of all residuals so as to eliminate outliers. The residuals were calculated as in Equation (1), and the minimum residual was identified as the smallest residual across all the mass pairs considered for a given composition. The two wind1 and wind2 trajectories are described in detail in Wollaeger et al. (2018). The two nuclear mass models considered are FRDM2012 and HFB24 (Möller et al. 2016; Pearson et al. 2014). The two nuclear fission models considered in our study are FRLDM (Mumpower et al. 2020) and “50/50,” a simple symmetric assumption that fission yields split into two identical nuclei. The fission rates for the simulations performed in previous work, labeled Panov+ (2010), are taken from Panov et al. (2010). The asterisk indicates the compositions used in creating the surrogate light curves used during parameter estimation (see Section 3). The reported Y_e values describe the neutron richness of just the dynamical ejecta component.

calculated from decaying the r -process composition from the `WinNet` code (Winteler et al. 2012). The contributions from these power sources are weighted by thermalization efficiencies first presented in Barnes et al. (2016; see Wollaeger et al. 2018 for a detailed description of the adopted nuclear heating). We use detailed opacity calculations from the tabulated binned opacities generated using the Los Alamos suite of atomic physics codes (Fontes et al. 2015, 2020). Our tabulated binned opacities are not calculated for all elements; therefore, we produce opacities for representative proxy elements by combining pure-element opacities of nuclei with similar atomic properties (Fontes et al. 2020). We use only the first four ion stages for each element in our light-curve calculations, as they are sufficient given the photospheric temperature of the kilonova ($T \sim 10^4$ K; Fontes et al. 2020, 2023). However, other studies have recently shown that higher ionization stages are important for a detailed treatment of early-time opacities (Banerjee et al. 2020, 2022, 2023). Our final `SuperNu` outputs are simulated kilonova spectra evaluated at 1024 equally log-spaced wavelength bins from 0.1 to 12.8 μm across 54 viewing angles spaced equally in $\cos\theta$ for $-1 \leq \cos\theta \leq 1$. These spectra are then post-processed into light curves assuming a source distance of 10 pc.

Our `SuperNu` simulations require discrete mass and average outflow velocity parameter inputs for the ejecta components. To sample our parameter space continuously during parameter inference, we require a continuous mapping of ejecta parameter inputs to kilonova light-curve outputs in the

form of a Gaussian process surrogate model. We built our surrogate model training library of ~ 450 kilonova light-curve simulations using iterative simulation placement guided by Gaussian process variance minimization. In other words, we placed new simulations in regions of parameter space where our interpolation rms uncertainty was largest. For simulation placement purposes, we only examined the uncertainty on the entire bolometric light curve rather than uncertainty at individual simulation times (see Ristic et al. 2022 for a full discussion on the creation of the simulation library).

Using Gaussian process regression interpolation in conjunction with our simulation library (Ristic et al. 2022), we created a continuous mapping of our four ejecta parameter simulation inputs (M_d, v_d, M_w, v_w) to a scalar output $M_{AB,\lambda}$ at some time t , angle θ , and wavelength λ . Because of the substantial dynamic range of our many outputs, we interpolate in AB magnitudes using the LSST *grizy* and Two Micron All Sky Survey *JHK* bands as our reference wavelengths. Our Gaussian process uses a squared-exponential kernel and a white-noise (diagonal) kernel. Unless otherwise noted, we quantify the performance of our interpolation with the rms difference between our prediction and the true value.

Combining our surrogate light curves and parameter inference code, we generated posteriors for the ejecta parameters of GW170817 given our model assumptions (Ristic et al. 2022). We perform four-dimensional Monte Carlo integration of the electromagnetic likelihood over our model’s four parameters using the EM_PE package (Ristic et al. 2023) to provide the likelihood and the RIFT adaptive Gaussian mixture model integrator to perform the integration (Wofford et al. 2022). The parameter estimation in this work, discussed in Section 2.3, follows the same methodology as in Ristic et al. (2022), with the additional composition-based prior constraint described in Section 2.2.

In creating our surrogate model light-curve training library, we considered only one dynamical ejecta composition and one wind ejecta composition, indicated by the asterisk in Table 1. With regard to constructing a composition-informed mass prior, the wind compositions in this work are unchanged from previous studies (Wollaeger et al. 2018; Korobkin et al. 2021; Ristic et al. 2022), while new considerations for dynamical ejecta compositions with different nuclear physics inputs were included in addition to the original dynamical composition used in prior studies. As a result of its ejection process, dynamical ejecta typically has a much lower electron fraction $Y_e \equiv (n_p)/(n_p + n_n)$, where n_p is the number of protons and n_n is the number of neutrons in the ejecta. A low electron fraction results in a higher availability of neutrons for capture during r -process nucleosynthesis and thus generally the creation of heavier elements such as lanthanides and actinides (Burbidge et al. 1957; Cameron 1957). Due to the dynamical ejecta’s dominance on the elemental abundance pattern compared to the relatively minimal contribution of the wind ejecta, we only present newly calculated compositions for dynamical ejecta in this work.

The compositions presented in this work were generated using two nuclear network codes: WinNet (Reichert et al. 2023) and PRISM (Sprouse et al. 2021). The dynamical and wind ejecta compositions considered here and in previous work (i.e., Wollaeger et al. 2018; Ristic et al. 2022) were generated using WinNet. Specifically, these are the wind1 and wind2

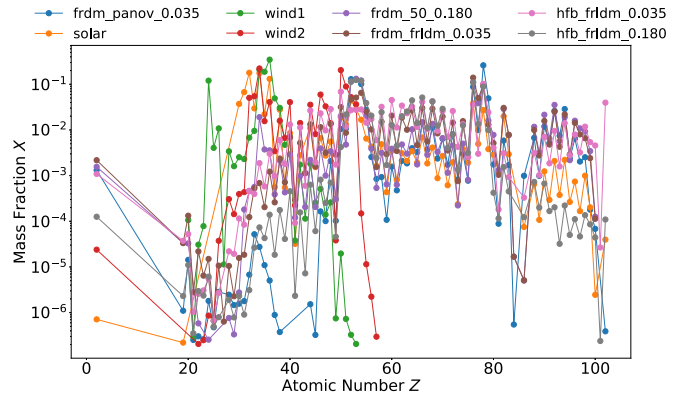


Figure 2. Unscaled mass fractions X as a function of atomic number Z for all single- Y_e compositions considered in this work. The labels pertaining to the dynamical ejecta compositions considered in this work indicate the nuclear mass model, fission model, and electron fraction Y_e used to generate the respective composition. The remaining labels indicate the solar and wind compositions. The wind1 and wind2 compositions do not extend to higher atomic numbers Z owing to their higher electron fractions $Y_e = 0.37$ and $Y_e = 0.27$, respectively.

compositions and the dynamical ejecta model using the Panov + (2010) fission model in Table 1.

The varied dynamical ejecta compositions new to this work were generated using PRISM. PRISM is a single-zone nuclear reaction network code that evolves an initial seed abundance of nuclei along a time–temperature–density thermodynamic trajectory, while allowing full flexibility with the input nuclear data (Sprouse et al. 2015). In this work, we use state-of-the-art nuclear reaction and decay rates that are calculated to be self-consistent with the nuclear mass model. Following from the thermodynamic trajectories of dynamical ejecta from neutron star merger simulations presented in Korobkin et al. (2012), all of our PRISM runs begin in nuclear statistical equilibrium at a temperature of 10 GK in the thermodynamic trajectory. All dynamical ejecta models presented in Table 1 with a fission model different from Panov+ (2010) were generated using PRISM.

The mass fractions of all the compositions considered in this work are shown in Figure 2. Figure 2 highlights the main difference between our wind ejecta compositions; the wind1 composition has very low mass fractions at the second r -process peak ($A \sim 130$), while a significant portion of the wind2 composition consists of elements around this peak.

2.2. Ejecta Prior Implied by r -process Observations

We seek to compare the combined mass fractions X_{sim} to the seemingly universal pattern of elements between the second and third r -process peaks (the “main” r -process; Cowan et al. 2021) observed among some of the oldest stars. This “ r -process universality” has been noted for iron-poor (or “metal-poor”) stars that show enhancements in the main r -process elements relative to their iron content in excess of 10 times the equivalent solar ratio. However, observationally derived abundances in metal-poor stars are necessarily elemental since the abundances are derived from atomic transitions in stellar spectra that are overall insensitive to atomic mass number. Except for a handful of elements, the detailed elemental distribution of r -process elements in metal-poor stars is observationally unknown. As a proxy for a representative example of the universal r -process, we use the well-studied

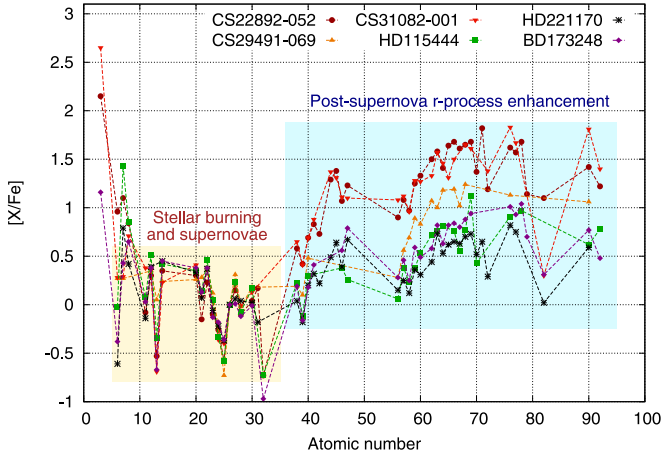


Figure 3. Elemental mass fraction ratios relative to iron of a sample of r -process-enriched metal-poor stars. $[X/Fe] > 0$ implies enhanced abundance of element X compared to the solar system with respect to iron. We assume all elements that are significantly enhanced compared to iron to have been introduced post-supernova, exclusively from neutron star mergers. The region of enhanced elements ($Z \geq 37$, highlighted in blue) is the focus of our comparison to solar composition. The iron-peak elements and supernova r -process are not strongly enhanced compared to solar (highlighted in yellow). Stellar elemental abundances are obtained from JINABase (Abohalima & Frebel 2018), with the respective stars reported in Westin et al. (2000), Hill et al. (2002), Cowan et al. (2002), Sneden et al. (2003), Ivans et al. (2006), and Hayek et al. (2009).

solar isotopic abundance pattern X_{\odot} , relying on previously published projections of the high- A elements into different neutron capture process contributions. Specifically, the r -process fractions presented in Arlandini et al. (1999) are used in conjunction with the total abundances from Sneden et al. (2008) to isolate the contribution to the solar abundances by the r -process.

Figure 3 shows the $[X/Fe]$ abundances of six metal-poor stars with r -process enhancements. The “[X/Fe]” notation means that each elemental ratio $\log \epsilon(X/Fe)$ is compared to the same elemental ratio in the solar abundance pattern.¹³ Stars with $[X/Fe] > 0$ are considered “enhanced” in that element relative to the solar system abundance. For many metal-poor stars, elements with $Z \geq 37$ have an enhanced abundance compared to the Sun. For this work, guided by the enhancement seen in elements $Z \geq 37$ in Figure 3 and with the assumption that iron was created during supernova nucleosynthesis, we assume that elements with $Z \geq 37$ originate *exclusively* from neutron star mergers. The trends of elements with $Z < 37$ are less clear; they are not uniformly enhanced in stars that are enhanced with the $Z \geq 37$ elements, likely pointing to multiple (nonmerger) origins for these elements.

In our SuperNu simulations, we adopt a two-component compositional model and vary the mass ratio of the two components: the dynamical (M_d) and wind (M_w) ejecta masses. Each component has a fixed isotopic abundance, computed via nucleosynthesis network (Winteler et al. 2012). Due to the fixed nature of the compositions, we weight each component’s composition, represented by mass fractions X_d and X_w , by the mass of the respective ejecta component, dynamical M_d and wind M_w , to introduce composition variation as a function of

component mass in the combined simulation mass fraction $X_{\text{sim}} = (M_d X_d + M_w X_w) / (M_d + M_w)$. For every isotope, the combined mass fraction X_{sim} is simply the mass-weighted sum of its mass fractions in the constitutive components. We varied our dynamical and wind component masses over a grid between $-3 \leq \log(M_{d,w}/M_{\odot}) \leq -1$, encompassing the most realistic ejecta masses predicted by numerical relativity simulations of neutron star mergers (Perego et al. 2014; Rosswog et al. 2017; Radice et al. 2018; Fernández et al. 2019; Miller et al. 2019; Nedora et al. 2021).

To account for isotopes of actinides with short decay timescales, we rescale the solar mass fractions of actinides $X_{\odot,Ac}$ to what they would have been at 1 day to better match the kilonova-timescale mass fractions used in our simulations. The rescaling is achieved by setting the 1-day solar actinide mass fractions to values that would decay to present-day values after 4.5 Gyr. The rescaled solar mass fractions are also mapped into a subset of representative elements used for SuperNu light-curve modeling as described in Section 2.1. Hereafter, any mention of the solar mass fraction pattern X_{\odot} refers to the 1-day rescaled and mapped mass fractions using data from Arlandini et al. (1999) and Sneden et al. (2008).

To get X_{\odot} and X_{sim} on the same relative scale, we introduce an offset $C_{\text{scale},Z}$ that shifts X_{\odot} down to comparable values for X_{sim} by matching the two mass fraction values at some element Z . To minimize how the choice of $C_{\text{scale},Z}$ affects our results, we integrate over the range of possible values of $C_{\text{scale},Z}$ introduced by scaling X_{\odot} and X_{sim} to matching values at different elements Z . This integration marginalizes over our uncertainty in $C_{\text{scale},Z}$, adopting a Gaussian prior on $\log(C_{\text{scale},Z})$ with mean $\mu = 0.08$ and variance $\sigma^2 = 0.695$. After integrating over $C_{\text{scale},Z}$, we are left with a single required choice of a new C value that sets the constrained scale at some element Z_{choice} such that $\log X_{\text{sim},Z_{\text{choice}}} = \log X_{\odot,Z_{\text{choice}}} - \log C$. We chose $Z_{\text{choice}} = 46$, as it is one of the elements present in all the dynamical, wind, and solar mass fractions. Shifting X_{\odot} to be on the same relative scale as X_{sim} and choosing a specific value of C at some Z_{choice} are both done solely for the purpose of calculating well-behaved residuals. While the scaling by C removes the constraint that $\sum_Z X_{\odot,Z} = 1$, this has no detrimental effects on our analysis, as we are interested exclusively in our compositions’ relative abundances.

As part of our assumption that elements $Z \geq 37$ were synthesized exclusively in neutron star mergers (see Figure 3), we only consider elements from $Z = 37$ up to and including $Z = 103$ when computing the residual $r(M_d, M_w)$ for all available elements in the solar abundance pattern $Z \in Z_{\odot}$ given a simulation with component masses M_d, M_w :

$$r(M_d, M_w) = \sum_{Z=37}^{103} \frac{(\log X_{\odot,Z} - \log C - \log X_{\text{sim},Z})^2}{2\sigma^2} - \frac{N (\log \bar{X}_{\text{sim}} - \log \bar{X}_{\odot})^2}{2\sigma^2 (1 + \sigma^2 / (N\sigma_C^2))} \quad (1)$$

where $r(M_d, M_w)$ is the residual for the given dynamical and wind mass pair used to calculate $X_{\text{sim}} = (M_d X_d + M_w X_w) / (M_d + M_w)$, Z is the element’s atomic number, $\log X_{\odot,Z}$ is the decimal logarithm of the solar mass fraction of element Z , $\log C$ is the decimal logarithm of the offset matching X_{\odot} to X_{sim} at $Z = 46$, $\log X_{\text{sim},Z}$ is the decimal logarithm of the simulation mass fraction of element Z in both components (if present), σ is

¹³ Definition: $[X/Fe] := \log \epsilon(X/Fe) - \log \epsilon(X/Fe)_{\odot}$, where $\log \epsilon(X) := \log_{10}(Y_X/Y_H) = \log_{10}(Y_X) + 12$, where Y_X is the abundance (mole fraction) of the element X.

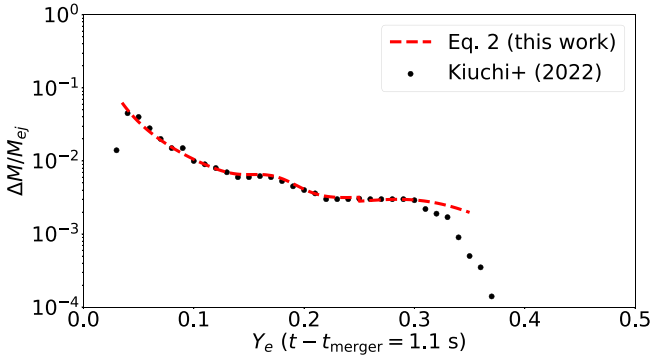


Figure 4. Re-created Y_e distribution for dynamical ejecta as presented in Figure 5 of Kiuchi et al. (2023). The analytic fit to the distribution, presented in Equation (2), is overlaid as a red line. The analytic fit was used to generate the Y_e -distribution compositions presented in Table 2.

the uncertainty on $\log X_{\text{sim}}$, σ_C is the uncertainty introduced by integrating out $C_{\text{scale,Z}}$, \bar{X}_{\odot} is the average solar mass fraction across all elements, \bar{X}_{sim} is the average simulation mass fraction across all elements, and N is the total number of elements considered.

We compute the residual between each of our composition models X_{sim} from Table 1 and the solar mass fraction pattern X_{\odot} using Equation (1). We consider component mass weights across a log-spaced grid with $-3 \leq \log(M_{d,w}/M_{\odot}) \leq -1$, with 50 masses for each component, resulting in a total of 2500 residuals per composition model. The scaled residual values $r - r_{\text{min}}$ are shown in the top panel of Figures 5 and 6, with r representing the residual calculated for each mass pair and r_{min} the lowest residual for all mass pairs considered for a given model.

Guided by numerical relativity simulations that suggest a distribution of Y_e values in neutron star ejecta (e.g., Miller et al. 2019; Most & Raithel 2021; Nedora et al. 2021; Kiuchi et al. 2023), we also analyze a selection of compositions derived from the Y_e distribution for dynamical ejecta presented in Figure 5 of Kiuchi et al. (2023). To calculate the mass weights for each Y_e value, we re-create the Y_e distribution with a piecewise analytic fit

$$\begin{aligned} \Delta M/M &= 0.05C(Y_e/0.04)^{-1.7} \\ &+ \frac{A}{\sqrt{(2\pi\sigma_1^2)}} e^{-0.5(Y_e-0.17)/\sigma_1^2} \\ &+ \frac{B}{\sqrt{(2\pi\sigma_2^2)}} e^{-0.5(Y_e-0.3)/\sigma_2^2} \end{aligned} \quad \text{with} \quad C = \begin{cases} 1 & Y_e \leq 0.25 \\ (0.04/Y_e)^{0.1} & Y_e > 0.25, \end{cases} \quad (2)$$

with fit parameters $A = 10^{-4}$, $B = 2 \times 10^{-4}$, $\sigma_1 = 0.02$, $\sigma_2 = 0.05$. A comparison of the fit to the Kiuchi et al. (2023) Y_e distribution is shown in Figure 4. Our fit begins to deviate from the distribution at $Y_e = 0.3$; this is of little concern, as less than 3% of the total ejecta mass is described by $Y_e > 0.3$.

For each Y_e -distribution composition, we run 10 nucleosynthesis simulations, evenly spaced between $0.035 \leq Y_e \leq 0.35$. The mass weight for each single- Y_e composition is calculated using Equation (2). Once all the weights are calculated, they are normalized such that their net contribution describes the total ejecta mass. The final Y_e -distribution

composition is the weighted sum of the abundances from the single- Y_e nucleosynthesis simulations. After the net Y_e -distribution composition is calculated, we repeat the same methodology as for the models presented in Table 1 to calculate mass ratios and residuals for each composition model.

2.3. Parameter Inference

As in many previous applications of Bayesian inference to infer parameters of kilonovae (Smartt et al. 2017; Villar et al. 2017; Coughlin et al. 2018, 2019; Breschi et al. 2021; Heinzel et al. 2021; Nicholl et al. 2021; Lukošiuete et al. 2022), we seek to compare the observed magnitudes x_i at evaluation points i (denoting a combination of band and time) to a continuous model that makes predictions $m(i|\theta)$ that depend on some model parameters θ . Bayes's theorem expresses the posterior probability $p(\theta)$ in terms of a prior probability $p_{\text{prior}}(\theta)$ for the model parameters θ and a likelihood $\mathcal{L}(\theta)$ of all observations, given the model parameters, as

$$p(\theta) = \frac{\mathcal{L}(\theta)p_{\text{prior}}(\theta)}{\int d\theta \mathcal{L}(\theta)p_{\text{prior}}(\theta)}. \quad (3)$$

Unless otherwise noted, for simplicity we assume that the source sky location, distance, and merger time are known. We adopt a uniform prior on the ejecta velocity $v/c \in [0.05, 0.3]$ and the two-dimensional prior discussed in Section 2.2 on the ejecta masses $m/M_{\odot} \in [0.001, 0.1]$.

We assume that the observations have Gaussian-distributed magnitude errors with presumed known observational (statistical) uncertainties σ_i , convolved with some additional unknown systematic uncertainty σ , so that our log-likelihood is

$$\ln \mathcal{L}(\theta) = -0.5 \sum_{i=1}^n \left[\frac{(x_i - m(i|\theta))^2}{\sigma_i^2 + \sigma^2} + \ln(2\pi(\sigma_i^2 + \sigma^2)) \right], \quad (4)$$

where the sum is taken over every data point in every band used in the analysis. For inference using our Gaussian process surrogate models, we set σ to the estimated Gaussian process model error. For a full discussion of our parameter inference considerations, see Ristic et al. (2022).

3. Results

For our two-component models, assuming that a single source like GW170817 dominates the observed solar r -process abundances, the inferred abundances from such mergers only depend on the mass ratio M_w/M_d . In other words, since in our study we emphasize only the relative and not absolute r -process abundances, motivated by considerable uncertainty in the binary neutron star merger rate, we therefore only use and constrain the abundance *ratios*. The relative abundances from a single channel only depend on the relative proportions of this channel; for our two-component model, this is simply dependent on M_w/M_d . Thus, for each set of initial assumptions—the composition of the dynamical ejecta (represented by the electron fraction Y_e), the presumed nuclear mass and fission model, and other details—our comparison with solar abundances necessarily constrains M_w/M_d narrowly around a preferred value unique to that model. We note that the abundances we are considering are effectively frozen out for the processes we are interested in at times later than $\mathcal{O}(1)$ s.

Table 2

Same as Table 1, Except Considering Dynamical Ejecta Compositions Derived from the Y_e Distribution Presented in Figure 5 of Kiuchi et al. (2023)

Mass Model	Fission Model	Wind Comp.	Mass Ratio (M_w/M_d)	Min. Residual (r_{\min})
FRDM2012	FRLDM	wind2	0.32	1467
FRDM2012	50/50	wind2	0.34	1809
FRDM2012	FRLDM	wind1	0.04	1854
HFB27	FRLDM	wind2	0.81	2433
HFB27	50/50	wind2	0.81	2548
FRDM2012	50/50	wind1	0.01	3242
HFB27	FRLDM	wind1	0.04	4080
HFB27	50/50	wind1	46.89	4609

Note. We also consider the HFB27 mass model in place of HFB24.

Tables 1 and 2 provide a list of models and their preferred M_w/M_d , in the sense that they minimize the residual mismatch with the solar abundances as calculated in Equation (1). With a few exceptions, most models prefer M_w/M_d substantially lower than order unity. In other words, most of our abundance comparisons suggest that less wind than dynamical ejecta would be required for GW170817-like mergers to reproduce the solar r -process abundances. These results are at odds with those found from other contemporary modeling (Coughlin et al. 2019; Kawaguchi et al. 2020; Almualla et al. 2021; Nicholl et al. 2021), as well as numerical relativity results (Perego et al. 2014; Radice et al. 2016; Dietrich et al. 2017; Shibata & Hotokezaka 2019; Nedora et al. 2021), which typically predict more post-merger (i.e., wind) mass ejection.

One particularly interesting result is that the lowest-residual single- Y_e composition in Table 1 agrees with X_\odot better than the Y_e -distribution composition with similar nuclear physics inputs. This result suggests that a single- Y_e approximation is adequate for computational simplicity in the context of nucleosynthesis calculations.

Without detailed elemental abundances from metal-poor stars, we rely on relative abundances to calculate the preferred ejecta mass ratio. This approach is subject to variation stemming from the chosen value of Z_{choice} at which the relative abundances are matched. In our study, the subset of possible values of Z_{choice} is set by the wind compositions, as these compositions synthesize fewer elements at $Z \geq 37$. Near this region, the dynamical and wind compositions are changing rapidly, both above and below. Furthermore, the two wind compositions we use both also change rapidly, as $Z \simeq 37$ is close to the maximum Z produced at some of our assumed values of Y_e . For example, while wind2 produces elements up to $Z \simeq 55$, wind1 produces very small quantities of elements above $Z \simeq 40$. As the value of Z_{choice} gets smaller, however, we encroach the region where our merger-only nucleosynthesis assumption begins to give way to stellar-burning and supernova nucleosynthesis as shown in Figure 3. Conversely, all our analyses neglect systematics associated with nonmerger contributions by assuming only r -process contributions from $Z > 37$.

To assess the sensitivity of our results to the value of Z_{choice} , we repeated our analysis for the specific array of Z values for which we have sufficiently compatible abundance patterns ($Z = [37, 38, 44-53]$). The exact preferred ratio for M_w/M_d does vary between our fiducial value of 0.47 for $Z_{\text{choice}} = 46$ up

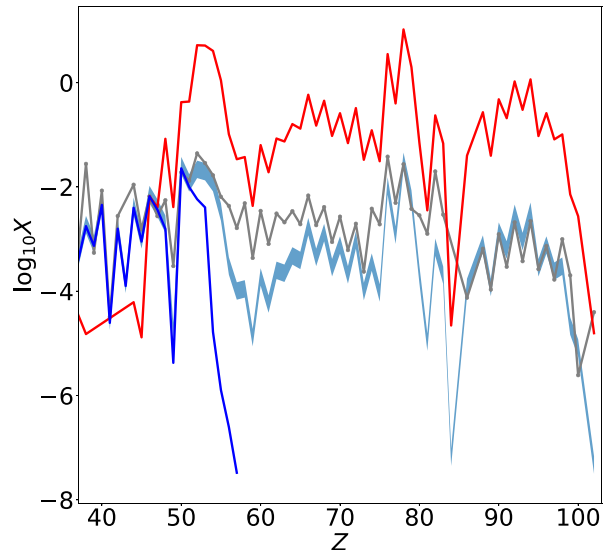
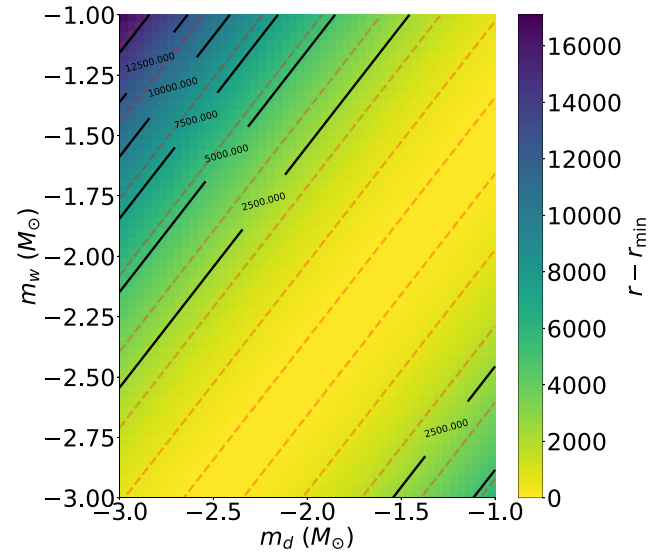


Figure 5. Top: 2D distribution of residuals calculated as in Equation (1) by comparing $\log X_\odot$ to $\log X_{\text{sim}}$ using the dynamical and wind compositions matching those in Ristic et al. (2022), represented by the asterisk in Table 1. The residual grid is composed of 50 mass values equally log-spaced between $-3 \leq \log M_\odot \leq -1$ for both dynamical and wind mass. The black lines indicate contours of equally spaced residual values. The dashed red lines indicate a wind-to-mass ratio of 1 and serve purely as a visual aid. Bottom: mass fractions of individual ejecta components compared to the best-fit mass fraction X_{sim} obtained from comparison to X_\odot . The red and blue lines are the initial unweighted dynamical (X_d) and wind (X_w) ejecta mass fractions, respectively, scaled by C to match the solar mass fraction at $Z = 46$. The gray line is the solar mass fraction X_\odot , and the blue shaded region is the 90% confidence interval for all the mass-weighted mass fractions $\log X_{\text{sim}}$. The dynamical ejecta mass fraction only exceeds $\log X = 0$ owing to the scale matching at $Z = 46$.

to around 2 for $Z_{\text{choice}} = 52$. We are therefore most confident that the two components contribute in comparable amounts, though the component that dominates overall is not definitively determined.

The top panel of Figure 5 shows the mass pair residuals for the composition and morphology assumptions considered in previous work (Ristic et al. 2022), denoted by the asterisk in Table 1. The yellow stripe indicating the lowest-residual region highlights the best-fitting ratio of wind-to-dynamical mass

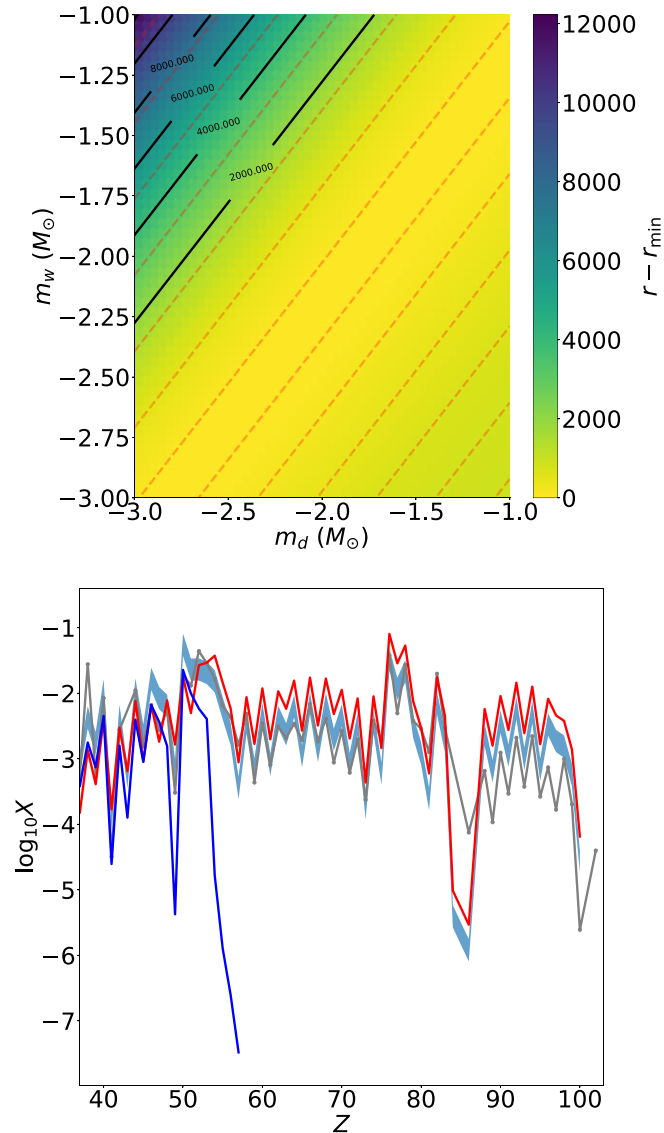


Figure 6. Top: same 2D distribution as described in Figure 5, except with the compositions that yielded the lowest residual in comparison to the solar abundance pattern X_{\odot} (top row of Table 1). Bottom: mass fractions of individual ejecta components compared to the best-fit mass fraction X_{sim} obtained from comparison to X_{\odot} . The line colors represent the same quantities as in Figure 5. The minimum residual was identified as the smallest residual across all the mass pairs considered for a given composition X_{sim} .

implied by the calculated residuals. This corresponds to the “Mass Ratio (M_w/M_d)” value recorded in Table 1.

The top panel of Figure 6 shows the best-fitting wind-to-dynamical mass ratio for the lowest-residual composition model presented in this work: dynamical ejecta with a composition characterized by the FRDM2012 mass model, FRLDM fission model, electron fraction $Y_e = 0.035$, and wind ejecta corresponding to the wind2 model. The bottom panels of Figures 5 and 6 show the solar mass fraction pattern X_{\odot} in gray, the dynamical and wind ejecta fixed composition mass fraction patterns X_d and X_w in red and blue, respectively, and the 90% confidence interval for the mass fraction pattern of the relevant composition model X_{sim} as the light-blue shaded region. The 90% confidence interval was calculated for the spread of possible mass fraction patterns that arose when scaling the fixed component compositions X_d (X_w) by the component mass

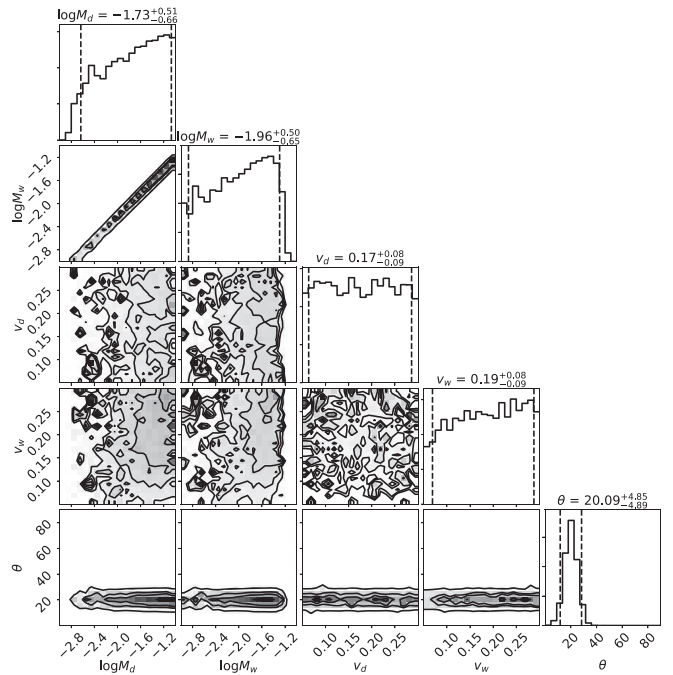


Figure 7. Posterior distributions created using only the 2D r -process prior presented in Figure 6, with no electromagnetic information provided during sampling besides constraints on the opening angle (see Troja et al. 2020 and references therein). We apply a scale factor in our likelihood calculation during inference to prevent underflow from the large residual values. Note the recovery of the yellow band of lowest-residual mass pairs from Figure 6 in the M_w vs. M_d panel, as well as the flat velocity posteriors stemming from the lack of velocity constraints introduced by our mass-focused prior. Residual small-scale substructure in the one- and two-dimensional marginal distributions reflects sample size artifacts.

M_d (M_w). Based on the good agreement shown in Figure 6, we adopt the associated two-dimensional likelihood versus M_d and M_w as a prior constraint on ejecta masses. In other words, we assume that GW170817 was produced from a representative member of a single population of kilonovae, which alone are responsible for the solar r -process abundance).

For each set of initial assumptions, the inferred constraint on M_w/M_d therefore also strongly constrains the ingredients powering the associated kilonova. For example, Figure 7 shows the results of inferring the parameters of GW170817, using only our prior constraints on M_w/M_d from the top panel of Figure 6 (and weak constraints on the binary orientation relative to our line of sight). Figure 8 shows how these constraints propagate into joint electromagnetic inference. The solid black contours show inferences derived without using constraints on M_w/M_d ; the red contours show inferences supplemented with this insight, for a specific set of initial assumptions. Figure 9 shows the light curves associated with the recovered posterior distributions presented in Figure 8. The inclusion of the composition prior results in much tighter model uncertainties compared to the light-curve fits in Ristić et al. (2022).

Each set of our input assumptions about ejecta composition and physics makes a prediction about r -process abundances. As shown by the last column in Tables 1 and 2, some of our input assumptions fit better than others. Given substantial systematic uncertainties associated with the many assumptions in our study, we approach these nominal residuals with considerable cautions. However, the minimum residuals presented in Tables 1 and 2 suggest that the wind2 model is a notably

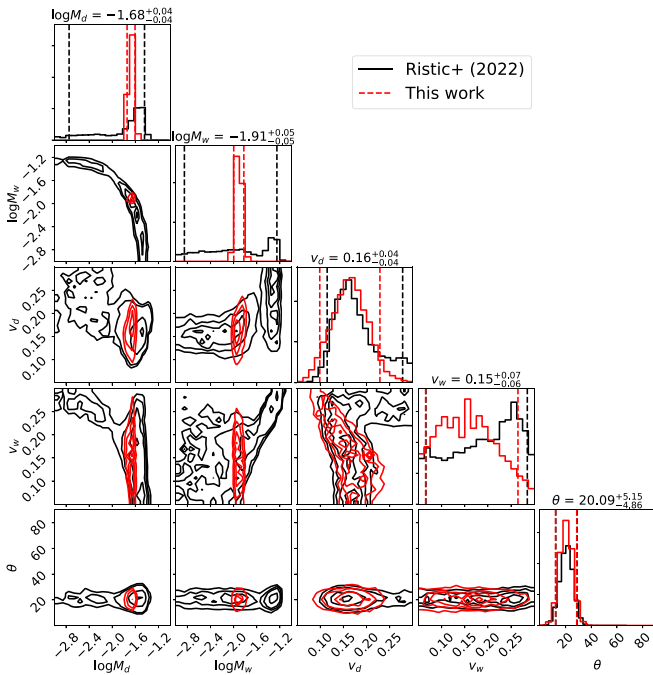


Figure 8. Posterior distributions for samples generated when using the *grizyJHK* bands considered in Ristic et al. (2022; black) and samples generated using the same bands along with the *r*-process prior from Figure 6 (red). The values reported at the top of each posterior distribution represent the inference results from this study. The composition prior effect is most evident in the wind mass posterior shift to lower ejecta mass.

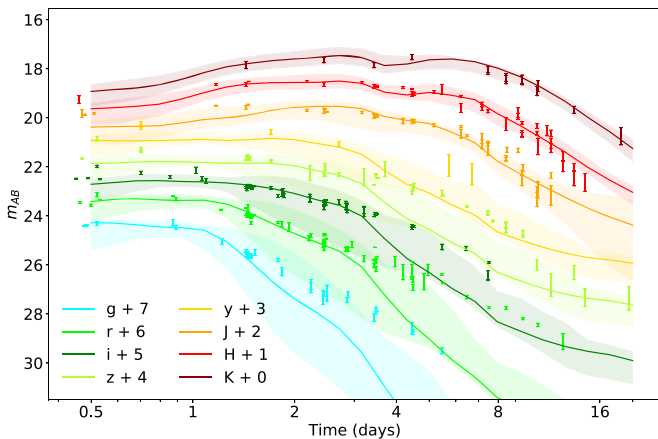


Figure 9. Broadband light-curve predictions for the ejecta parameters recovered in Figure 8. The inclusion of the composition-based mass prior (top panel of Figure 6) reduces model prediction uncertainty compared to previous predictions (Ristic et al. 2022).

better fit to the solar mass fraction pattern, consistent with similar findings in previous studies (Evans et al. 2017). The nearly distinct separation of the two wind models’ lowest residuals implies that the wind1 model is less indicative of *r*-process nucleosynthesis from neutron star mergers; however, our work neglects consideration of lighter *r*-process elements ($Z \leq 37$), which disfavors compositions with higher Y_e like wind1. More importantly, the separation between the models also implies that new models for the wind ejecta composition need to be considered in comparison to the wind2 model. The results of Tables 1 and 2 indicate the need for further studies involving updated wind ejecta composition modeling informed by GRMHD disk simulations (Miller et al. 2019).

The results of Tables 1 and 2 also depend strongly on the assumption that neutron star mergers are the *dominant* *r*-process mechanism for the creation of elements with $Z \geq 37$ (see Figure 3 and Section 2.2), which may not be the case; see, e.g., Ji et al. (2019) and references therein.

Our method as stated also assumes that a narrow distribution of mergers in total mass $M_{\text{tot}} = M_1 + M_2$ dominates nucleosynthesis yields. While self-evidently consistent with the binary neutron star population inferred from the merging Galactic neutron star binaries, this assumption could even still hold for a wider binary neutron star population as suggested by gravitational wave observations, if ejecta are (as expected) suppressed for the most massive mergers with large M_{tot} .

Another caveat that presents limitations to our results is that we only incorporate very specific wind1 and wind2 compositions. There can be a broad variety of compositions permitted for electron fractions $Y_e > 0.20$ owing to varying hydrodynamic conditions. An extensive study of these compositions, along with the tests of how much they can be considered “representative” of their respective components, is beyond the scope of this work.

Our results can further be improved by incorporating the observed higher variability of the lighter *r*-process abundances between the first and second peaks, compared to the universal pattern between the second and third *r*-process peaks. The lighter *r*-process as observed in metal-poor stars exhibits variation on the order of 1 dex, while the “strong” *r*-process pattern varies by only about 0.3 dex (Cowan et al. 2021). An investigation with more accurate numbers based on careful statistical analysis of observations will be the subject of future studies (Farouqi et al. 2022).

Finally, we note that we cannot ignore the bias introduced by the dynamical ejecta composition of the surrogate kilonova light curves presented in Ristic et al. (2022). While the constraints imposed by the *r*-process abundance prior indeed shift the recovered parameters as in Figure 8, there still remains some contribution to the parameter estimation stemming from the surrogate models having been trained on a different dynamical ejecta composition. In other words, our surrogate light curves were trained using the ejecta compositions in Table 1 labeled with an asterisk. Although the primary contribution to the parameter inference in this work comes from the prior discussed in Section 2.2, some bias from the surrogates’ original compositions is unavoidable.

4. Conclusion

We have presented an approach for incorporating nuclear-physics-based composition effects as a prior for our kilonova parameter inference framework. Identifying a self-consistent electromagnetic and elemental signature from kilonova models enables us to make sharper conclusions about any specific kilonova’s ejecta. Moreover, our calculations provide a Bayesian evidence, assessing how well both observations can be fit independently and together. Our approach, by virtue of postulating the falsifiable assumption that neutron star mergers are the sole site of *r*-process nucleosynthesis, may therefore provide a new avenue to directly test whether BNS mergers are the primary source of *r*-process enrichment, using any potential star as a prototype (e.g., the Sun or a metal-poor, *r*-process-enriched example).

While our self-consistent approach will remain impactful as pertinent inputs improve, of course the quantitative numerical

results shown here are merely illustrative, given substantial systematics. Our calculations rely on physical models of BNS mergers, ejecta, and the r -process abundance signature in solar and metal-poor stars, all of which have substantial and widely investigated systematics. To highlight one important potential source of systematics in this approach, we considered a range of models with varying nuclear physics inputs, and, given the assumptions discussed above, the best-fitting model appears to be the one with FRDM2012 nuclear mass, FRLDM fission, $Y_e = 0.035$ (extreme neutron richness in dynamical ejecta), moderately neutron-rich wind ejecta, producing inferred dynamical and wind ejecta masses of $M_d \sim 0.021$ and $M_w \sim 0.012$ and corresponding to a relatively low mass ratio: $M_w/M_d = 0.47$. Our consideration of additional dynamical ejecta compositions, when compared to solar abundances, has indicated that the mass ratio between the two ejecta components is larger than what was implied by previous inference ($M_w/M_d = 0.24$). However, our conclusions should be taken with care, since the number of input compositions considered was quite limited.

We have also shown that the inferred mass ratio stemming from a comparison of r -process elemental abundances is highly sensitive to the input nuclear physics. For our preferred wind2 model, variations in the dynamical ejecta composition can change the recovered wind-to-dynamical ejecta mass ratio by a factor of ~ 4.3 . For the wind1 model, the inferred mass ratio can change by a factor of ~ 4689 , although this is largely due to the assumptions made in this work. While we focused on selected nuclear physics systematics, we have identified several areas meriting further study, including propagating different choices for nuclear physics uncertainties into our parameter inferences; examining whether more complex composition (e.g., Y_e), angular, or velocity distributions in the outflow can mimic these effects; and employing better prototypes than the Sun for a potential r -process signature.

Even allowing for extremely conservative systematic uncertainties on our inputs (e.g., assuming that M_w/M_d 's optimal value is well localized between 0.1 and 10), these prior abundance constraints should still provide useful insight into kilonova ejecta modeling. For instance, this framework of kilonova surrogates with abundance priors can be used as a constraint to identify merger simulations that produce consistent properties.

With the introduction of this composition-based prior, we are able to continue using our existing kilonova surrogate model and parameter inference frameworks while updating our inference priors to match contemporary results in the literature. The ability to update our mass prior using the underlying properties of kilonova models, without requiring expensive simulations (outside of nuclear network outputs), allows us to inexpensively and rapidly update our parameter inference results.

In this work, we have considered fiducial initial conditions for the outflow, including composition, without allowing for correlations induced by the fact that both the composition and outflows are initialized by binary neutron star mergers. In future work, we will explore self-consistent initialization from merger properties, in particular exploring the effects of binary mass ratio and neutron star remnant lifetime, which should have a significant impact on the ejecta amount and composition

(Kullmann et al. 2022; Vassh et al. 2022; Fujibayashi et al. 2023).

Current prospects for the detection of kilonovae in LIGO's fourth observing run indicate the possibility of an additional detection with potential for electromagnetic follow-up (Colombo et al. 2022). With enough luck, spectral observations of a secondary kilonova with JWST could indicate strong line features indicative of the presence of particular elements. While these line features would not give a complete isotopic distribution of r -process from kilonovae, they would further constrain which elements must be present in simulated ejecta compositions.

Acknowledgments

R.O.S., M.R., and E.M.H. acknowledge support from NSF AST 1909534. R.O.S. acknowledges support from NSF AST 2206321. E.M.H. acknowledges additional support for this work by NASA through the NASA Hubble Fellowship grant HST-HF2-51481.001, awarded by the Space Telescope Science Institute, which is operated by the Association of Universities for Research in Astronomy, Inc., for NASA, under contract NAS5-26555. C.J.F., C.L.F., M.R.M., O.K., R.W., and T.M.S. were supported by the US Department of Energy through the Los Alamos National Laboratory. Los Alamos National Laboratory is operated by Triad National Security, LLC, for the National Nuclear Security Administration of the US Department of Energy (contract No. 89233218CNA000001). Research presented in this article was supported by the Laboratory Directed Research and Development program of Los Alamos National Laboratory under project No. 20190021DR. This research used resources provided by the Los Alamos National Laboratory Institutional Computing Program, which is supported by the US Department of Energy National Nuclear Security Administration under contract No. 89233218CNA000001.

Appendix A Sensitivity Study

Due to the variability in mass ratios as nuclear physics assumptions change (see Tables 1 and 2), we conduct a sensitivity study to identify whether certain elements have significant impact on the recovered mass ratio. We modify our best-fitting case with mass model FRDM2012, FRLDM fission, a fixed Y_e of 0.035, and a wind2 composition by choosing specific elements to be omitted during the residual calculation. The results are shown in Table 3. Most notably, the inclusion (or lack thereof) of actinides strongly influences the preferred mass ratio, dropping it from an average of $M_w/M_d \approx 0.3$ to $M_w/M_d \approx 0.1$. We also note elements of interest $Z = 86$ and $Z = 100$, which, when removed during the residual calculation, yield the highest and lowest mass ratios, respectively. Our sensitivity to the actinides indicates that our choice of mass ratio during inference should be used with caution. Specifically, the mass prior can provide additional parameter constraints when used self-consistently with the input model nuclear physics but can have detrimental effects when applied incorrectly. Despite some sensitivity to the actinide composition, our central conclusion that $M_w/M_d < 1$ remains robust.

Table 3
Sensitivity Study Results Using a Leave-one-out Approach with Specific Elements, the Lanthanides, the Actinides, and Both Lanthanides and Actinides

Z_{removed}	M_w/M_d	Residual
37	0.32	1466
38	0.31	1354
39	0.33	1464
40	0.31	1463
41	0.32	1438
42	0.32	1466
43	0.32	1467
44	0.32	1461
45	0.32	1463
47	0.32	1466
48	0.32	1464
49	0.32	1458
50	0.27	1466
51	0.29	1464
52	0.33	1444
53	0.33	1460
54	0.35	1466
55	0.33	1466
56	0.34	1454
57	0.34	1412
58	0.33	1464
59	0.32	1465
60	0.33	1466
61	0.33	1466
62	0.33	1466
63	0.33	1467
64	0.33	1464
65	0.33	1456
66	0.33	1466
67	0.33	1463
68	0.33	1466
69	0.32	1459
70	0.33	1466
71	0.32	1467
72	0.32	1464
73	0.33	1463
74	0.33	1464
75	0.34	1428
76	0.37	1464
77	0.33	1459
78	0.36	1464
79	0.33	1464
80	0.34	1447
81	0.34	1406
82	0.35	1439
83	0.33	1459
84	0.32	1467
85	0.32	1467
86	0.38	1112
87	0.32	1467
88	0.31	1437
89	0.3	1413
90	0.32	1443
91	0.31	1433
92	0.32	1447
93	0.31	1450
94	0.32	1455
95	0.31	1452
96	0.31	1425
97	0.31	1416
98	0.31	1436
99	0.28	1454
100	0.26	1312
101	0.32	1467

Table 3
(Continued)

Z_{removed}	M_w/M_d	Residual
102	0.36	1332
103	0.32	1467
La	0.44	1372
Ac	0.14	775
La+Ac	0.1	651

Note. In each case, the elements in the Z column are removed from consideration during the residual calculation. Interesting cases include $Z = 86$, which significantly reduces the calculated residual and yields the largest ratio of M_w/M_d , and $Z = 100$, which yields the lowest ratio. We find that we are particularly sensitive to the actinides in our compositions, as the mass ratio dramatically changes when they are removed from the residual calculation.

Appendix B Derivation of Marginalized Abundance Likelihood

We assume that abundance measurement uncertainties are uncorrelated and individually normally distributed in $\log X$. To marginalize considerable uncertainty in the overall normalization of X , we marginalize over uncertainty in this normalization, yielding the effective residual Equation (1). In this appendix, we briefly outline the derivation of this marginal log-likelihood.

We consider a signal $y = f_A + F_B \lambda_B + \epsilon$ generated by superposing two known models f_A and $F_B \lambda_B$ with parameters λ_A , λ_B on top of Gaussian noise ϵ . In this expression, y is an N -dimensional vector (i.e., our log abundance data), ϵ is normally distributed with mean zero and inverse covariance γ , and $F\lambda$ are linear operations transforming model parameters λ into predictions for y . We want to marginalize out the impact of the linear model F_B (here, the average abundance). For this model, the log-likelihood has the form (up to an overall normalization constant)

$$-2 \ln(L_{P_B}(\lambda_B)) = (f + F_B \lambda_B - y)^T \gamma (f + F_B \lambda_B - y) + \lambda_B^T \Gamma_B \lambda_B, \quad (\text{B1})$$

where we use a normal prior for λ_B with mean zero and inverse covariance Γ_B . To marginalize over λ_B , we complete the square in this Gaussian log-likelihood versus λ_B and then integrate over λ_B , arriving at (up to an overall normalization constant)








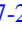


$$-2 \ln L_{\text{marg}} = (f - y)^T G (f - y) \quad (\text{B2})$$

$$G = [\gamma - \gamma F_B (F_B^T \gamma F_B + \Gamma_B)^{-1} F_B^T \gamma]. \quad (\text{B3})$$

In our case, $F_B = (1, 1, 1, \dots, 1) \equiv \mathbf{v}$ is a unit column vector (the same prediction for all element abundances, set to agree with the parameter λ_B), $\gamma = \mathbf{1}/\sigma^2$ is the assumed-common uncertainty in each (log) abundance measurement, and $\Gamma_B = 1/\sigma_B^2$ is our assumed uncertainty in the common matching value. As a result, $F_B^T \gamma F_B = N/\sigma^2$ (a constant, not a matrix), $F_B^T \gamma F_B + \Gamma_B = N/\sigma^2 + 1/\sigma_B^2$, and the combination appearing in the second term of G has the form

$$\gamma F_B (F_B^T \gamma F_B + \Gamma_B)^{-1} F_B^T \gamma = \frac{1}{\sigma^4} \mathbf{v} \mathbf{v}^T \frac{1}{\sigma_B^{-2} + N/\sigma^2}. \quad (\text{B4})$$

ORCID iDs

Marko Ristić  <https://orcid.org/0000-0001-7042-4472>
 Erika M. Holmbeck  <https://orcid.org/0000-0002-5463-6800>
 Ryan T. Wollaeger  <https://orcid.org/0000-0003-3265-4079>
 Oleg Korobkin  <https://orcid.org/0000-0003-4156-5342>
 Elizabeth Champion  <https://orcid.org/0000-0002-7901-4100>
 Richard O’Shaughnessy  <https://orcid.org/0000-0001-5832-8517>
 Chris L. Fryer  <https://orcid.org/0000-0003-2624-0056>
 Christopher J. Fontes  <https://orcid.org/0000-0003-1087-2964>
 Matthew R. Mumpower  <https://orcid.org/0000-0002-9950-9688>
 Trevor M. Sprouse  <https://orcid.org/0000-0002-4375-4369>

References

- Abbott, B. P., Abbott, R., Abbott, T. D., et al. 2017, *ApJL*, 848, L13
 Abomalima, A., & Frebel, A. 2018, *ApJS*, 238, 36
 Almualla, M., Ning, Y., Bulla, M., et al. 2021, arXiv:2112.15470
 Arlandini, C., Käppeler, F., Wisshak, K., et al. 1999, *ApJ*, 525, 886
 Banerjee, S., Tanaka, M., Kato, D., et al. 2022, *ApJ*, 934, 117
 Banerjee, S., Tanaka, M., Kato, D., & Gaigalas, G. 2023, arXiv:2304.05810
 Banerjee, S., Tanaka, M., Kawaguchi, K., Kato, D., & Gaigalas, G. 2020, *ApJ*, 901, 29
 Barnes, J., Kasen, D., Wu, M.-R., & Martínez-Pinedo, G. 2016, *ApJ*, 829, 110
 Barnes, J., & Metzger, B. D. 2022, *ApJL*, 939, L29
 Barnes, J., Zhu, Y. L., Lund, K. A., et al. 2021, *ApJ*, 918, 44
 Bartos, I., & Márka, S. 2019, *ApJL*, 881, L4
 Breschi, M., Perego, A., Bernuzzi, S., et al. 2021, *MNRAS*, 505, 1661
 Burbidge, E. M., Burbidge, G. R., Fowler, W. A., & Hoyle, F. 1957, *RvMP*, 29, 547
 Cameron, A. G. W. 1957, *PASP*, 69, 201
 Colombo, A., Salafia, O. S., Gabrielli, F., et al. 2022, *ApJ*, 937, 79
 Coughlin, M. W., Dietrich, T., Doctor, Z., et al. 2018, *MNRAS*, 480, 3871
 Coughlin, M. W., Dietrich, T., Margalit, B., & Metzger, B. D. 2019, *MNRAS*, 489, L91
 Cowan, J. J., Sneden, C., Burles, S., et al. 2002, *ApJ*, 572, 861
 Cowan, J. J., Sneden, C., Lawler, J. E., et al. 2021, *RvMP*, 93, 015002
 Cowperthwaite, P. S., Berger, E., Villar, V. A., et al. 2017, *ApJL*, 848, L17
 Dietrich, T., Bernuzzi, S., Ujevic, M., & Tichy, W. 2017, *PhRvD*, 95, 044045
 Eichler, D., Livio, M., Piran, T., & Schramm, D. N. 1989, *Natur*, 340, 126
 Evans, P. A., Cenko, S. B., Kennea, J. A., et al. 2017, *Sci*, 358, 1565
 Farouqi, K., Thielemann, F. K., Rosswog, S., & Kratz, K. L. 2022, *A&A*, 663, A70
 Fernández, R., Tchekhovskoy, A., Quataert, E., Foucart, F., & Kasen, D. 2019, *MNRAS*, 482, 3373
 Fontes, C. J., Fryer, C. L., Hungerford, A. L., Wollaeger, R. T., & Korobkin, O. 2020, *MNRAS*, 493, 4143
 Fontes, C. J., Fryer, C. L., Wollaeger, R. T., Mumpower, M. R., & Sprouse, T. M. 2023, *MNRAS*, 519, 2862
 Fontes, C. J., Zhang, H. L., Abdallah, J., Jr., et al. 2015, *JPhB*, 48, 144014
 Fraser, J., & Schönrich, R. 2022, *MNRAS*, 509, 6008
 Frebel, A., Christlieb, N., Norris, J. E., et al. 2007, *ApJL*, 660, L117
 Fujibayashi, S., Kiuchi, K., Wanajo, S., et al. 2023, *ApJ*, 942, 39
 Goriely, S., Bauswein, A., & Janka, H.-T. 2011, *ApJL*, 738, L32
 Hayek, W., Wiesendahl, U., Christlieb, N., et al. 2009, *A&A*, 504, 511
 Heinzel, J., Coughlin, M. W., Dietrich, T., et al. 2021, *MNRAS*, 502, 3057
 Hill, V., Plez, B., Cayrel, R., et al. 2002, *A&A*, 387, 560
 Hulse, R. A., & Taylor, J. H. 1975, *ApJL*, 195, L51
 Ivans, I. I., Simmerer, J., Sneden, C., et al. 2006, *ApJ*, 645, 613
 Ji, A. P., Drout, M. R., & Hansen, T. T. 2019, *ApJ*, 882, 40
 Kawaguchi, K., Shibata, M., & Tanaka, M. 2020, *ApJ*, 889, 171
 Kiuchi, K., Fujibayashi, S., Hayashi, K., et al. 2023, *PhRvL*, 131, 011401
 Korobkin, O., Rosswog, S., Arcones, A., & Winteler, C. 2012, *MNRAS*, 426, 1940
 Korobkin, O., Wollaeger, R. T., Fryer, C. L., et al. 2021, *ApJ*, 910, 116
 Kulkarni, S. R. 2005, arXiv:astro-ph/0510256
 Kullmann, I., Goriely, S., Just, O., et al. 2022, *MNRAS*, 510, 2804
 Lattimer, J. M., & Schramm, D. N. 1974, *ApL*, 192, L145
 Lattimer, J. M., & Schramm, D. N. 1976, *ApJ*, 210, 549
 Li, L.-X., & Paczyński, B. 1998, *ApJL*, 507, L59
 The LIGO Scientific Collaboration, The Virgo Collaboration, Abbott, B. P., et al. 2017c, *ApJL*, 848, L12
 The LIGO Scientific Collaboration, The Virgo Collaboration, Abbott, B. P., et al. 2017a, *ApJL*, 850, L39
 The LIGO Scientific Collaboration, The Virgo Collaboration, Abbott, B. P., et al. 2017b, *ApJL*, 850, L40
 The LIGO Scientific Collaboration, the Virgo Collaboration, Abbott, B. P., et al. 2017d, *PhRvL*, 119, 161101
 Lorusso, G., Nishimura, S., Xu, Z. Y., et al. 2015, *PhRvL*, 114, 192501
 Lukošiusė, K., Raaijmakers, G., Doctor, Z., Soares-Santos, M., & Nord, B. 2022, *MNRAS*, 516, 1137
 Macias, P., & Ramirez-Ruiz, E. 2019, *ApJL*, 877, L24
 Metzger, B. D. 2019, *LRR*, 23, 1
 Metzger, B. D., & Berger, E. 2012, *ApJ*, 746, 48
 Metzger, B. D., Martínez-Pinedo, G., Darbha, S., et al. 2010, *MNRAS*, 406, 2650
 Miller, J. M., Ryan, B. R., Dolence, J. C., et al. 2019, *PhRvD*, 100, 023008
 Möller, P., Sierk, A. J., Ichikawa, T., & Sagawa, H. 2016, *ADNDT*, 109, 1
 Most, E. R., & Raithel, C. A. 2021, *PhRvD*, 104, 124012
 Mumpower, M. R., Jaffke, P., Verriere, M., & Randrup, J. 2020, *PhRvC*, 101, 054607
 Nedora, V., Bernuzzi, S., Radice, D., et al. 2021, *ApJ*, 906, 98
 Nicholl, M., Berger, E., Kasen, D., et al. 2017, *ApJL*, 848, L18
 Nicholl, M., Margalit, B., Schmidt, P., et al. 2021, *MNRAS*, 505, 3016
 Panov, I. V., Korneev, I. Y., Rauscher, T., et al. 2010, *A&A*, 513, A61
 Pearson, J. M., Chamel, N., Fantina, A. F., & Goriely, S. 2014, *EPJA*, 50, 43
 Perego, A., Rosswog, S., Cabezón, R. M., et al. 2014, *MNRAS*, 443, 3134
 Pian, E., D’Avanzo, P., Benetti, S., et al. 2017, *Natur*, 551, 67
 Radice, D., Galeazzi, F., Lippuner, J., et al. 2016, *MNRAS*, 460, 3255
 Radice, D., Perego, A., Hotokezaka, K., et al. 2018, *ApJL*, 869, L35
 Reichert, M., Winteler, C., Korobkin, O., et al. 2023, arXiv:2305.07048
 Ristic, M., Champion, E., O’Shaughnessy, R., et al. 2022, *PhRvR*, 4, 013046
 Ristic, M., Champion, E., & O’Shaughnessy, R. 2023, EM_PE, Zenodo, doi:10.5281/zenodo.8226050
 Roberts, L. F., Kasen, D., Lee, W. H., & Ramirez-Ruiz, E. 2011, *ApJL*, 736, L21
 Rosswog, S. 2015, *IJMPD*, 24, 1530012
 Rosswog, S., Feindt, U., Korobkin, O., et al. 2017, *CQGra*, 34, 104001
 Rosswog, S., Korobkin, O., Arcones, A., Thielemann, F.-K., & Piran, T. 2014, *MNRAS*, 439, 744
 Savchenko, V., Ferrigno, C., Kuulkers, E., et al. 2017, *ApJL*, 848, L15
 Shen, S., Cooke, R. J., Ramirez-Ruiz, E., et al. 2015, *ApJ*, 807, 115
 Shibata, M., & Hotokezaka, K. 2019, *ARNPS*, 69, 41
 Siqueira Mello, C., Spite, M., Barbuy, B., et al. 2013, *A&A*, 550, A122
 Skúladóttir, Á., & Salvadori, S. 2020, *A&A*, 634, L2
 Smartt, S. J., Chen, T. W., Jerkstrand, A., et al. 2017, *Natur*, 551, 75
 Sneden, C., Cowan, J. J., & Gallino, R. 2008, *ARA&A*, 46, 241
 Sneden, C., Cowan, J. J., Lawler, J. E., et al. 2003, *ApJ*, 591, 936
 Sneden, C., Preston, G. W., McWilliam, A., & Searle, L. 1994, *ApJL*, 431, L27
 Sprouse, T., Mumpower, M., Surman, R., & Aprahamian, A. 2015, APS Meeting, 2015, EA.097
 Sprouse, T. M., Mumpower, M. R., & Surman, R. 2021, *PhRvC*, 104, 015803
 Symbalisty, E., & Schramm, D. N. 1982, *ApL*, 22, 143
 Tanaka, M., Kato, D., Gaigalas, G., & Kawaguchi, K. 2020, *MNRAS*, 496, 1369
 Tanvir, N. R., Levan, A. J., González-Fernández, C., et al. 2017, *ApJ*, 848, L27
 Taylor, J. H., & Weisberg, J. M. 1982, *ApJ*, 253, 908
 Thielemann, F. K., Eichler, M., Panov, I. V., & Wehmeyer, B. 2017, *ARNPS*, 67, 253
 Troja, E., Piro, L., van Eerten, H., et al. 2017, *Natur*, 551, 71
 Troja, E., van Eerten, H., Zhang, B., et al. 2020, *MNRAS*, 498, 5643
 Vassh, N., McLaughlin, G. C., Mumpower, M. R., & Surman, R. 2022, arXiv:2202.09437
 Villar, V. A., Guillochon, J., Berger, E., et al. 2017, *ApJL*, 851, L21
 Westin, J., Sneden, C., Gustafsson, B., & Cowan, J. J. 2000, *ApJ*, 530, 783
 Winteler, C., Käppeli, R., Perego, A., et al. 2012, *ApJL*, 750, L22
 Wofford, J., Yelkar, A., Gallagher, H., et al. 2022, arXiv:2210.07912
 Wollaeger, R. T., Korobkin, O., Fontes, C. J., et al. 2018, *MNRAS*, 478, 3298
 Wollaeger, R. T., & van Rossum, D. R. 2014, *ApJS*, 214, 28
 Zhu, Y. L., Lund, K. A., Barnes, J., et al. 2021, *ApJ*, 906, 94